EPJ Web of Conferences **114**, 02072 (2016)
DOI: 10.1051/epjconf/201611402072

Measurement of Liquid Film Thickness via Light Absorption and Laser Tomography

M.A. Mendez[1,2,a], L. Németh[1,], and J-M. Buchlin[1]

[1] *Von Karman Institute for Fluid Dynamics, Environmental and Applied Fluid Dynamics Department*
[2] *Université Libre de Bruxelles, Département d' Aéro-Thermo-Mécanique, Faculté des Sciences Appliquées*

Abstract.
This paper presents film thickness measurement over a vertical falling liquid film, carried out with Light Absorption (LAbs) and a 2D laser tomography techniques known as Level Detection and Recording (LeDaR). The presented test cases are in the low Reynolds regime ($Re = 1 - 8$) and include undisturbed conditions, i.e. constant flow rate, and inlet-forced conditions, i.e. flow rate pulsing at frequencies in the range $f_p = 12 - 18Hz$. The liquid used is Dipropilene Glycol (DPG), with Kapitza number $Ka = 4.6$. The results include average film thickness in the steady case, wave celerity and wave profile in the forced conditions. All the measurements are scaled using the Skhadov scaling, to facilitate the comparison with analytical low-dimensional models. Both LAbs and LeDaR techniques are presented in detail, including calibration, uncertainties and data processing aspects.

1 Introduction

Falling liquid films are encountered in many applications, including the coating processes of paint, paper or galvanizing industries, and the heat and mass transfer equipment of process industries. These flows are inherently unstable and prone to develop interface instabilities which are crucial in any application: they can limit the quality of coated products or enhance heat and mass transfer.

Besides the industrial concerns, falling liquid films motivated a large amount of fundamental research since the seminal work of Kapitza [1], as liquid films are in fact laminar flows amenable to analytical treatment. Several simplified models have been developed over the years [2–4]. These models aim to reduce the complexity of the governing Navier-Stokes (N-S) equations by identifying a stream-wise length scale ($[x]$) much larger than the thickness scale ($[h]$), to define a reordering parameter $\varepsilon = [h]/[x] \ll 1$ which weights the forces governing the film flow: gravity, viscosity, inertia and surface tension. Neglecting terms above a given order p (i.e. $\propto \varepsilon^p$) leads to model analytically tractable, yet capable of describing the film dynamics. This separation of scales ($[x] \gg [h]$), achieved via the Shkadov scaling presented in Sec.5, is the fundamental framework of any analytical model.

Little attention, however, has been paid to a clear definition of the conditions under the separation of scales is possible. As discussed in Sec.5, this depends on the liquid properties. In particular, on the ratio between the capillary length scale $l_\sigma = \sqrt{\sigma/\rho g}$ and the viscosity length scale $l_\nu = \sqrt[3]{\nu^2/g}$, regrouped in a dimensionless number known as Kapitza number ($Ka = l_\sigma^2/l_\nu^2$). For low Ka liquids (e.g. organic oils or paints, with $Ka = O(1)$) separation of scales is not possible, since $\varepsilon \approx 1$. An experimental validation of these analytical models, however, requires 2D or 3D film thickness measurements with high spatial and temporal resolution [5–8], and few authors have reported detailed thickness measurements at low Ka.
Krantz & Goren ([9], $Ka = 3.4$) focused on the experimental prediction of natural instability inception, by measuring whether introduced disturbances were amplified or damped. Moran *et al* ([10], $Ka = 18.4$) proposed an extensive characterization of a Nusselt flow down to an inclined plane, in terms of averaged thickness and averaged velocity profiles. Nguyen & Balakotaiah ([11], $Ka = 6-22$) analyzed large amplitude waves on a low Kapitza liquid, but their single-point measurements do not allow for a complete insight into the travelling wave profile. Several cases at $Ka = 14$ and $Ka = 85$ have been presented by Charogiannis *et al* [12], who combined the thickness measurement with velocity measurement within the liquid.

This paper focuses on the experimental characterization of 2D waves traveling over a vertical falling liquid film of Dipropilene Glycol (DPG, $Ka = 4.6$), having $\rho = 1023 \pm 0.1\%[kg/m^3]$, $\mu = 87.5 \pm 1\%[cSt]$ $\sigma = 32 \pm 2\%[mN/m]$, in the range of Reynolds number $Re = q/\nu = 1 - 8$, being q the flow rate per unit width. The conditions analyzed include undisturbed regime and inlet forced regime, with superimposed pulsing flow rate at frequencies $f_p = 12 - 18Hz$. Time resolved, 2D and 3D film thickness measurements were performed using two measurement techniques. The first technique is the light absorption (LAbs), implemented in the 3D version used in

[a] e-mail: mendez@vki.ac.be

[17–19]; the second technique is an adaptation of a visualization method based on planar laser-induced fluorescence (PLIF) and image processing, referred to as level detection and recording (LeDaR, [23–25]). In the LAbs technique the film thickness is retrieved by measuring the intensity of the light transmitted through the liquid film. Developed as a point-wise technique, using photodiods or photomultipliers as light receivers [14, 15], the LAbs has later become a full field technique using digital video cameras and basic image processing operations [17–19]. While this method can provide high spatial and temporal resolution, its main limitation is in the assumption that the light transmittance is solely linked to light absorption, disregarding spurious effects such as light refraction, reflection or scattering.
In the LeDaR technique the film thickness is retrieved via digital processing of flow visualizations images. In these images the contrast liquid-background is enhanced using planar laser-induced fluorescence (PLIF) of a dye diluted in the liquid and an optical band-pass filter on the camera's objective. The key difference between this approach and other LIF-based methods such as in [20–22] is that the intensity of the fluorescence emission is not related to the film thickness, but only serves visualization purposes. As a result, the measurement requires no calibration. The image processing technique used to detect the interface varies according to the complexity of the analysed configuration. Examples of these approaches are proposed in [27–31] and in [12], where it is successfully combined with PIV velocity measurements within the liquid.

The next section presents the VKI facility and its operation in steady and unsteady condition. Sec.3 and Sec.4 reviews, respectively, the LAbs and the LeDaR techniques. Sec.5 briefly presents the measurement scaling according to the most popular scaling approach used in the literature of liquid film modeling: the Shkadov scaling. Sec.6 presents the experimental results, Sec.7 the conclusions.

2 Liquid film facility

The VKI liquid film facility is sketched in figure 1. It consists of a closed loop where the liquid falls along a vertical test section (1), is collected in a tank (2) and re-circulated into a pneumatic chamber (5) through an inlet line (4), by a volumetric pump (3, Pollard PR40). The pump is a rotative vane pump, which introduces a negligible temperature rise, avoiding the need of a heat exchanger. The liquid temperature was monitored in the test section and in the tank, and remained constant at $21.7^oC \pm 1\%$ during the tests presented in Sec.6.

In the pneumatic chamber, the liquid motion is minimized splitting both the input and the by-pass flow rates into four parts, positioning the inlet line $15cm$ below the liquid level, and hosting a large liquid volume ($18l$) during the experiment. This allows to maintain the liquid surface flat, and to control the hydrostatic head of the liquid flow by monitoring the rotational speed of the pump and the opening of the by-pass line. The volume of the liquid gives to the system a high inertia, to simplify the regulation of the facility and allow the user to set a constant level during the tests. Moreover, the chamber is pressurized from an inlet line (7), equipped with a pressure regulator, and discharges in atmosphere through an outlet line (8). A deflecting frame (9) avoids the impingement of the incoming air on the liquid interface within the chamber. The opening of the lines 7-8 is controlled by two butterfly valves (detail A), mounted with 90^o phase delay on the shaft of an electric motor (Maxon EC-4pole 45).

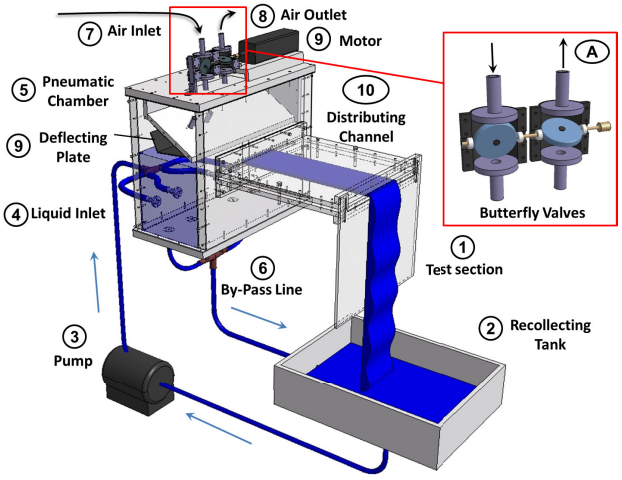

Figure 1: Sketch of the VKI liquid Film Facility All components are manufactured in ®PLEXIGLAS, with $1^{1/4} inch$ copper pipes for the connections 4-6.

In the steady operation mode, the motor is off, both valves are open, and a constant chamber pressure is settled by the upstream pressure regulator. In the unsteady operation mode, the motor opens and closes lines 7 and 8 periodically, producing two charge and discharge phases at every round, thus a pressure pulsation in the chamber.

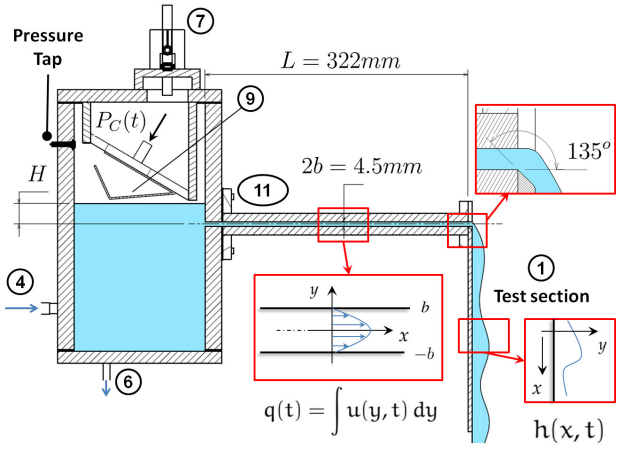

Figure 2: Facility Cross Section. The pressure pulsation $P_C(t)$ produces a flow rate pulsation $q(t)$, resulting in a wavy liquid film $h(x,t)$. A smooth connection between channel and test section prevents liquid detachment.

As the film thickness adhering the walls is considerably thinner than in the investigated areas, this interruption has no appreciable effects on the film thickness. This can

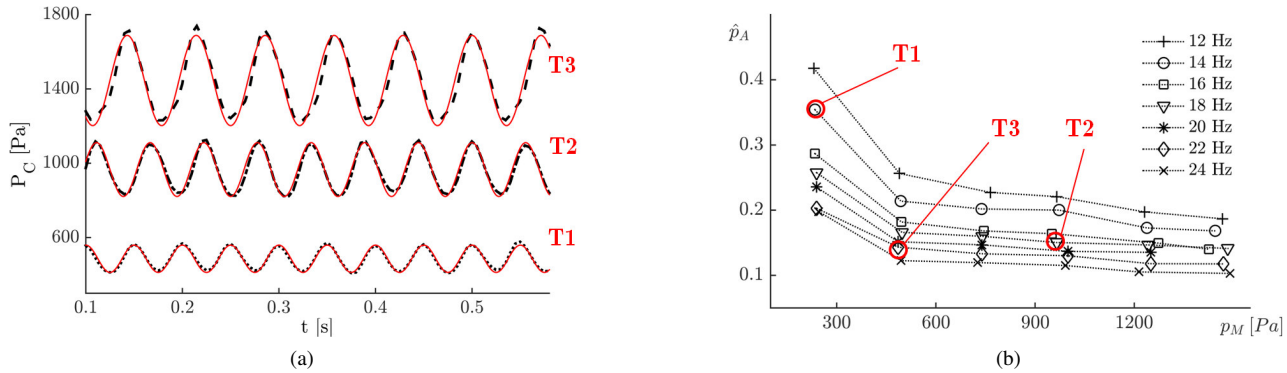

Figure 4: Pressure measurements in the pneumatic chamber. Figure 4a: examples of pressure signals $P_C(t)$ acquired from the pressure transducer at sampling $f_s = 800Hz$. Figure 4b: relative pressure amplitude $\hat{p}_A(p_M, f)$ curves for seven frequencies, six mean pressures.

be observed in the shape of the 3D liquid edges forming in the two sides of film, shown in figure3: no appreciable difference appears between the open (right) and closed (left) sides.

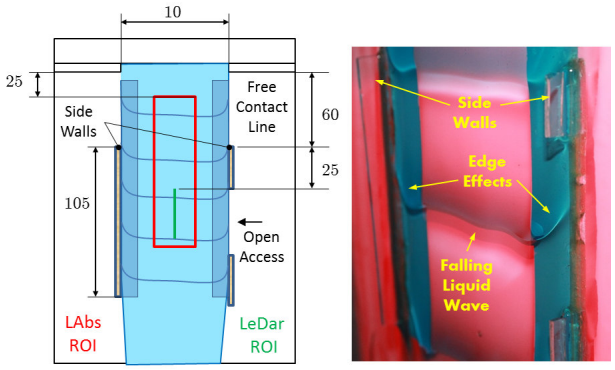

Figure 3: Test section front view, with measurements ROIs, and picture of a traveling wave during the test. The test section is illuminated by diffused red light, as described in section 3. The 3D lateral edges are unaffected by the open access in one of the side walls.

figure4a shows three examples of pressure signals $P_C(t)$, measured in the pneumatic chamber. On each of these signals it is fitted, in red, a harmonic pulsating pressure having mean value p_M, frequency f_p and amplitude p_A. The user controls the mean pressure p_M, through the pressure regulator in the inlet line, and the pulsation frequency f_p, through the motor speed $\omega_m = 4\pi f_p$. The pressure amplitude p_A, on the other hand, depends on the facility line-cavity behavior. As shown in figure 4b, the relative pressure amplitude $\hat{p}_A = p_A/p_M$ decreases asymptotically when increasing p_M and f_p.

Since the liquid flow in the channel is incompressible, 2D, and fully developed, the governing equation is linear thus the liquid flow rate per unit width q is the superimposition of a mean flow q_M, sustained by the mean pressure p_M, and an oscillatory component $q_A \sin(2\pi f_p - \phi)$, sustained by the oscillating pressure $p_A \sin(2\pi f_p)$. Referring to the sketch in figure 2, the liquid flow reaching the test section is governed by the x-wise momentum equation:

$$\frac{\partial u}{\partial t} = -\frac{1}{\rho}\frac{\partial p}{\partial x} + \nu\frac{\partial^2 u}{\partial y^2} \ . \tag{1}$$

As the total pressure is $p(t) = P_C(t) + \rho g H$ and the pressure drop is linear, the pressure gradient term reads:

$$-\frac{\partial p(t)}{\partial x} = -\left(\frac{P_M}{L} + \frac{p_A}{L}\cos(2\pi\, f_p t)\right), \tag{2}$$

where $P_M = p_M + \rho g H$ is the mean pressure head.
The momentum equation in eq.1 is conveniently rescaled via the following reference quantities: $\hat{y} = y/b$, $\hat{x} = x/L$, $\hat{u} = u/(P_M b^2/\mu L)$, $\hat{P} = P/P_M$, $\hat{t} = t/(2\pi f_p)$, obtaining:

$$\mathcal{W}^2\frac{\partial \hat{u}}{\partial \hat{t}} = -\frac{\partial \hat{p}}{\partial \hat{x}} + \frac{\partial^2 \hat{u}}{\partial \hat{y}^2} = -\left(1 + \hat{P}_A\cos(\hat{t})\right) + \frac{\partial^2 \hat{u}}{\partial \hat{y}^2} \ , \tag{3}$$

where eq.2 has been introduced. The only dimensionless number controlling the channel flow response is the Womersley number $\mathcal{W} = b\sqrt{\omega/\nu}$ ([32–34]).
The steady solution of eq.3, related to the mean flow, is the steady Poiseuille flow:

$$\hat{u}_M(\hat{y}) = \frac{1}{2}\left(1 - \hat{y}^2\right) \Longrightarrow \hat{q}_M = \int_{-1}^{1}\hat{u}_M(\hat{y})d\hat{y} = \frac{2}{3} \tag{4}$$

from which, reversing the scaling, the mean Reynolds number Re_M reads:

$$Re_M = \frac{q_M}{\nu} = \frac{2b^3}{3\rho\nu^2}\left(\frac{\rho g H + p_M}{L}\right) \tag{5}$$

The harmonic component of eq.3 can be obtained analytically in terms of a periodic, variable separated, complex solution $\tilde{u}(\hat{y}, \hat{t}) = \tilde{f}(\hat{y})e^{i\hat{t}}$ which trasforms eq.3 into a simple ordinary differential equation. The results, as shown in [35, 36], is the real part $\hat{u}_A = \mathbb{R}(\tilde{u})$:

$$\hat{u}_A(\hat{y}, \hat{t}) = \mathbb{R}\left\{\left(1 - \frac{\cosh(\mathcal{W}\sqrt{i}\,\hat{y})}{\cosh(\mathcal{W}\sqrt{i})}\right)\frac{i\,\hat{P}_A}{\mathcal{W}^2}\,e^{i\hat{t}}\right\} . \tag{6}$$

The corresponding flow rate amplitude can therefore be linked to a modulation term $\mathcal{T}$ which only depends on the Womersley number and the dimensionless pressure oscillation $\hat{P}_A$:

$$\hat{q}_A = \frac{1}{\cos(\hat{t} - \hat{\phi})} \int_{-1}^{1} \hat{u}_A(y,t) d\hat{y} \; = \mathcal{T}(\mathcal{W})\, \hat{P}_A \qquad (7)$$

from which, reversing the scaling, the amplitude of the Reynolds pulsation Re_A reads:

$$Re_A = \frac{q_A}{\nu} = \frac{3}{2} \mathcal{T}(\mathcal{W})\, \hat{P}_A\, Re_M \qquad (8)$$

figure 5 shows the modulation function $\mathcal{T}$ obtained analytically from eq.6 (Th), together with the results of CFD laminar simulations for three relative pressure amplitudes $(\hat{P}_A = 0.2 - 0.3 - 0.6)$ and frequency in the range $10 - 30 Hz$ [36]. The strength of the flow rate pulsation is hereinafter measured in terms of $\zeta = Re_A / Re_M$.

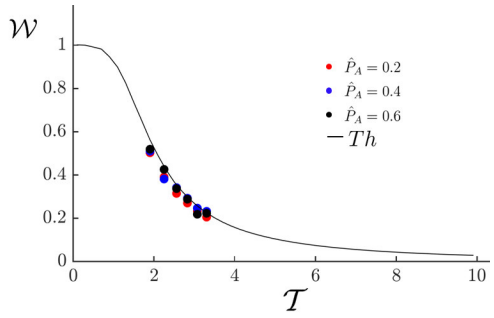

Figure 5: Modulation function $\mathcal{T}$ as a function of the Womersley number $\mathcal{W}$ produced by the pressure pulsation in the VKI Facility in figure 1. Comparison of CFD results and analytical derivation [36].

3 Light Absorption (LAbs)

The light absorption relates the instantaneous thickness distribution $h(x,y,t)$ with the amount of light absorbed from a back-lighting source, using the well known Beer-Lambert's law:

$$h(x,z,t) = \frac{1}{\gamma_g}\, ln\left(\frac{I_0(x,z)}{I(x,z,t)}\right) = \frac{A(x,z,t)}{\gamma_g} \qquad (9)$$

Where γ_g is the light extinction coefficient of the liquid, determined via calibration, $I_0(x,z)$ is the back-light intensity, referred to as *Reference Image*, $I(x,z,t)$ is the transmitted light intensity trough the liquid film, referred to as *Trasmittance Image*. The dimensionless quantity $A = ln(I_0/I)$ is referred to as *Absorbance*. The absorption coefficient γ_g is the average over the total spectrum of light captured by the receiver, and it is a function of the temperature. Light absorption is typically enhanced diluting in the liquid small concentration of colourant dye whose absorbance spectrum matches the emission spectrum of the light source. The colourant concentration c is thus a key variable affecting the technique's sensitivity and its influence is hereinafter analyzed. As for the temperature influence, its effects are canceled by performing calibration and measurements in the same conditions.

3.1 LAbs Test Section

The light absorption (LAbs) test section is sketched in figure 6. The light source (1) consists of two arrays with 4x4 LEDs of $\approx 0.7\,W$ each, with 90% emittance in the range $636 \pm 26\mu m$. They are placed $10\,cm$ behind a $3mm$ thick screen Opal ®PLEXIGLAS (2), which diffuses the light over the test section (3), to which it is attached. The receiver (4) is a rolling shutter $16bits$ CMOS camera (Hamamatsu ORCA-Flash4.0), synchronized with the LEDs, to acquire at $200Hz$ with a resolution of $500x2048pixels$.

The synchronization is achieved operating the camera in free running mode, with the camera controlling the LEDs so that the light flash occurs when the rolling shutter exposes the whole sensor. As a result, the *Reference* image $I_0(x,z)$ is determined with an uncertainty of 0.5% and no light flickering problems arise. A red absorbing colourant, the blue methlyene, is diluted in the DPG and an optical band-pass filtered $(640 \pm 40\mu m)$ is installed on the $50mm$ camera's objective, to limit the camera sensitivity to the portion of spectra in which absorption takes place.

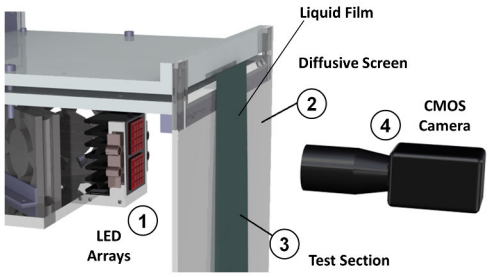

Figure 6: Light Absorption (LAbs) Test Section: LEDs (1) and screen (2) to back-light the test section (3) with diffuse, monochromatic light. A CMOS camera (4), to measure the attenuation of light produced by the liquid film.

3.2 LAbs Calibration and Data Processing

The LAbs calibration consists in evaluating the scaling factor $M[pixel/mm]$ and measuring the global extinction coefficient γ_g. The scaling factor is obtained by binarizing an image containing pattern of circles and extracting the diameter via standard morphology operations. In the LAbs measurement, it is typically $M = 19.6 pixel/mm \pm 1\%$. The extinction coefficient is measured using a calibrating vat and positioning the set up horizontally. Figure 7 sketches the calibration step and shows a typical absorbance profile. The absorbance profile is computed from the gray scale reference video $I_0(x,y,t)$, taken with an empty vat, and the gray scale transmittance video $I(x,y,t)$, taken with the vat filled with liquid. The corresponding absorbance image $A = ln(\bar{I}_0/\bar{I})$ is obtained from the time averages of

the videos $\bar{I}_0$ and $\bar{I}$. The absorption image is spatially filtered with a low-pass Gaussian and the average profile is fitted via linear regression. The camera alignment error can be corrected by rotating the image so as to have a zero gradient component $\partial A/\partial y = 0$.

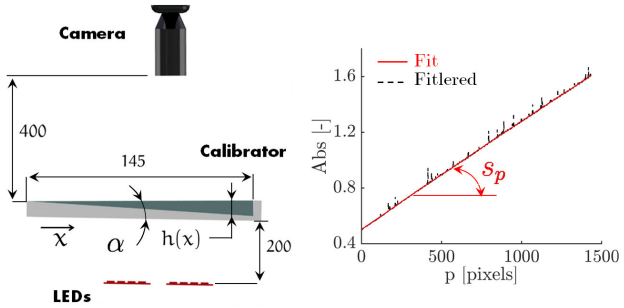

Figure 7: Calibrator of the LAbs measurement: calibrating vat and typical absorbance curve.

The absorption coefficient is retrieved from the vat slope $s_x = \tan(\alpha)$, the slope of the absorption profile in the image s_p, and the image scaling factor $M = x/p$, using eq. 9:

$$\gamma_g = \frac{A(x)}{h(x)} = \frac{s_p \cdot x\,/M}{x \cdot s_x} = \frac{s_p}{M \cdot s_x} \tag{10}$$

Figure 8 shows the linear dependency of the global absorption coefficient for the low colourant concentration used.

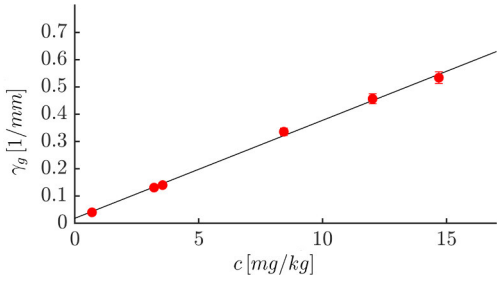

Figure 8: Extinction coefficient γ_g as a function of blue methylene diluted in DPG in mg/kg. The concentration range selected is sufficiently low to let the linearity in eq.9 hold.

3.3 LAbs Uncertainties and Sensitivity Analysis

The sensitivity–and the uncertainty– analysis of the LAbs measurement $\mathcal{U}_h(\gamma_p, A)$, as a function of the extinction coefficient and the absorbance, can be obtained from eq.9:

$$\mathcal{U}_h = \sqrt{\frac{\mathcal{U}_A^2}{\gamma_p^2} + \frac{A^2\,\delta\mathcal{U}_{\gamma_g}^2}{\gamma_g^4}}\,, \tag{11}$$

and depends on the absorbance and the extinction coefficient uncertainty $\mathcal{U}_A$ and $\mathcal{U}_{\gamma_g}$. In particular, the absorbance uncertainty δA depends on the measured gray scale transmittance I and reference I_0 images. From eq.9 it is:

$$\mathcal{U}_A = \sqrt{\left(\frac{\mathcal{U}_I}{I}\right)^2 + \left(\frac{\mathcal{U}_{I_0}}{I_0}\right)^2} \tag{12}$$

$$\approx \sqrt{\frac{\mathcal{U}_I^2}{I_0^2}\left(e^{2A}+1\right)} \tag{13}$$

using eq. 9 and assuming that $\mathcal{U}_I \approx \mathcal{U}_{I_0}$. This equation highlights an exponential growth of the uncertainty as the absorbance –thus the liquid thickness or the concentration– increases. The relative uncertainty of the light intensity $\mathcal{U}_I/I_0$ modulates this growth and represents the most important parameter. The synchronization camera-LED in this works gives $\mathcal{U}_I/I_0 = 0.15\%$. The uncertainty of the extension coefficient $\mathcal{U}_{\gamma_p}$, on the other hand, does not depend on the operating condition but only on the calibration. From eq.10 it is:

$$\mathcal{U}_{\gamma_p} = \sqrt{\left(\frac{\mathcal{U}_{s_p}}{M s_x}\right)^2 + \left(\frac{s_p\,\mathcal{U}_M}{M^2 \cdot s_x}\right)^2 + \left(\frac{s_p\,\mathcal{U}_{s_x}}{M \cdot s_x^2}\right)^2} \tag{14}$$

and leads to a relative uncertainty of $\mathcal{U}_{\gamma_g}/\gamma_g = 2\%$. Introducing eq.14 and eq.12 in eq.11 gives the thickness uncertainty as a function of the thickness and the extinction coefficient. The results are collected in figure 9.

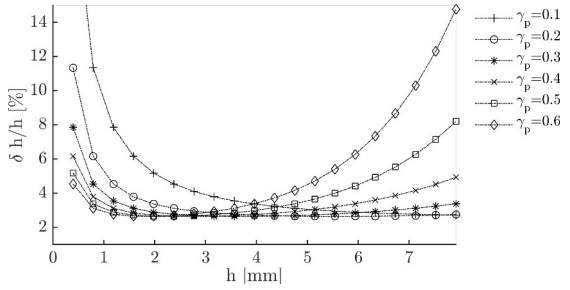

Figure 9: Relative uncertainty $\delta h/h$ as a function of the liquid thickness h for the different extinction coefficients γ_g, thus colourant concentrations.

It is evident that the choice of the extinction coefficient, thus the colourant concentration, depends on the film thickness range of interest: high concentrations are suited for thinner films while the reverse is true for low concentrations. As this work considers film thickness ranges $h = 1 - 6mm$, a colourant concentration of $c = 15mg/kg \pm 1\%$ was chosen, leading to $\gamma_g = 0.55mm^{-1} \pm 2\%$.

An example of LAbs measurement and processing is detailed in figure 10. The image processing only consists in converting the reference image I_0 and the transmittance image I into double precision array and use equation 9. The resulting thickness maps are low pass filtered using the fast smoothing spline method from [37], in order to remove the high frequency noise due to entrained micro bubbles without smoothing the liquid film thickness gradients.

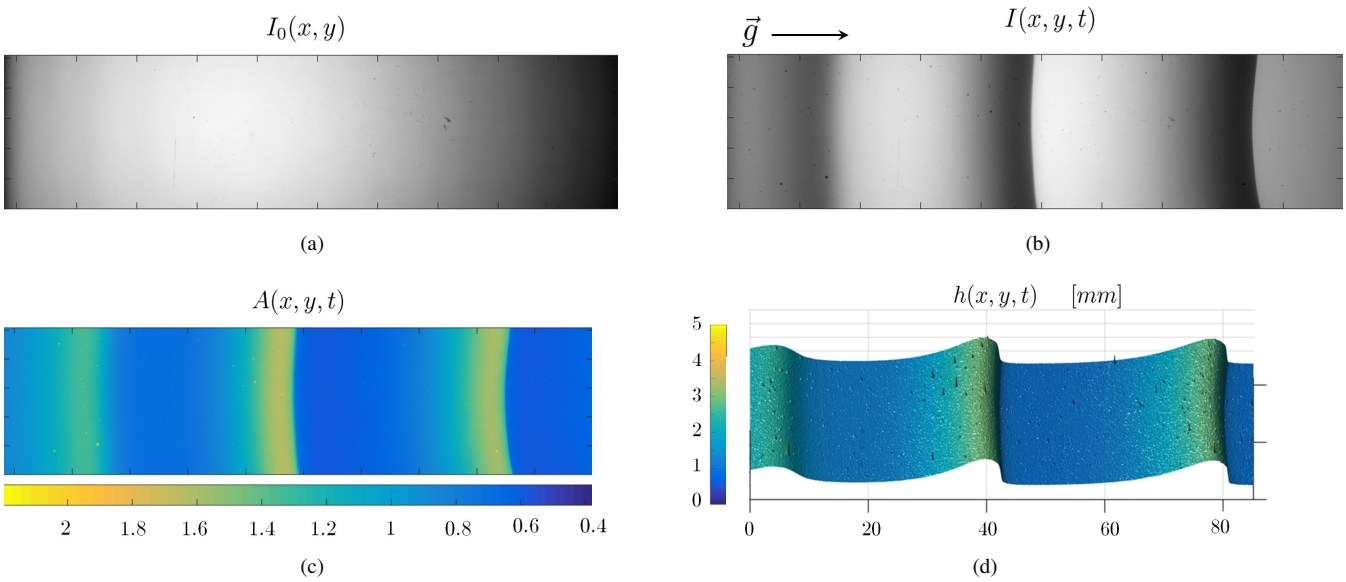

Figure 10: Image processing for LAbs measurement: the reference image $I_0(x,y)$ (in a), taken with the dry test section, is divided by the transmittance image $I(x,y,t)$ (in b) to compute the absorbance image $A(x,y,t) = ln(I_0/I)$. The corresponding instantaneous thickness contourmap, computed from Beer-Lambert's law (in d).

4 Level Detection and Recording (LeDaR)

The Level Detection and Recording (LeDaR) is an image processing technique developed at the von Karman Institute to extract air-liquid interfaces from laser tomography images ([23–25]). Other versions of the method have been independently developed in the literature ([27–31]). This method uses the planar laser induced fluorescence as a contrast enhancement tool and detects the liquid interface via image processing techniques, either via gradient-based methods (typically convolution with Sobel-like kernels) or via segmentation-based methods (typically Otsu's binarization preceded by histogram equalization). However, as the liquid waves observed in this work have larger amplitude and curvature than those measured in literature with this method, none of the two approaches proved successful. The main challenge is that the high interface curvature acts as a lens focusing light within a narrow region below the wave crest, hindering the uniformity of the illumination in the liquid domain. To overcome the problem, the routine presented combines directional image recontrasting with standard gray scale gradient analysis.

4.1 LeDaR Test Section

The LeDaR test section is sketched in figure 11. An optical bench (1) produces and direct a laser sheet towards the test section (2). A CMOS camera (3, Hamamatsu ORCA-Flash 4.0), equipped with 350mm zoom lens and an optical high pass filter (> 570μm) allows to visualize the laser induced fluorescence. The laser source is a continuous argon laser (Stability 2017, Spectra Physics); the diluted die is Rhodamine B with a concentration of 20mg/kg.

As for the light absorption measurement, the liquid flow lateral edges are defined by the lateral contact lines:

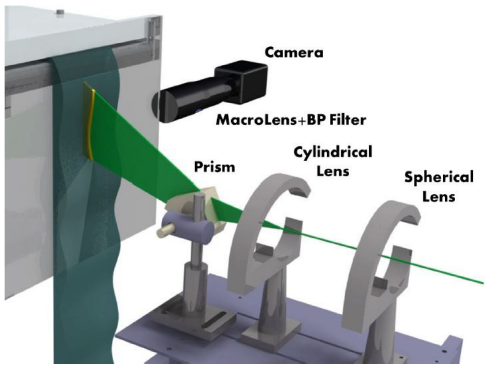

Figure 11: LeDaR setup: plane laser sheet, fluorescent dye diluted in the liquid, video camera. As for the LABS, the test section wall is wet before the test, to let the lateral flow boundaries defined by the liquid contact-line.

no wall nor boundaries are placed between the focal plane and the camera's objective which visualizes the illuminated plane through the liquid film. Contrary to the set ups in [23–25], no index-matching methods are therefore used. An example snapshot is shown in figure 12a. The video consists of a sequence of $n_T = 1000$, 16$bits$ gray scale images with $400 \times 2048 pixels$ resolution, sampled at $f_s = 200Hz$.

4.2 LeDaR Calibration and Data Processing

The calibration, performed in the dry test section, consists in evaluating the wall position and the scaling factor, using a pattern of circles. The scaling factor in the images was $M = 61 pixel/mm \pm 1\%$; the wall line was set as zero thickness with a typical alignment error of 1^o. No

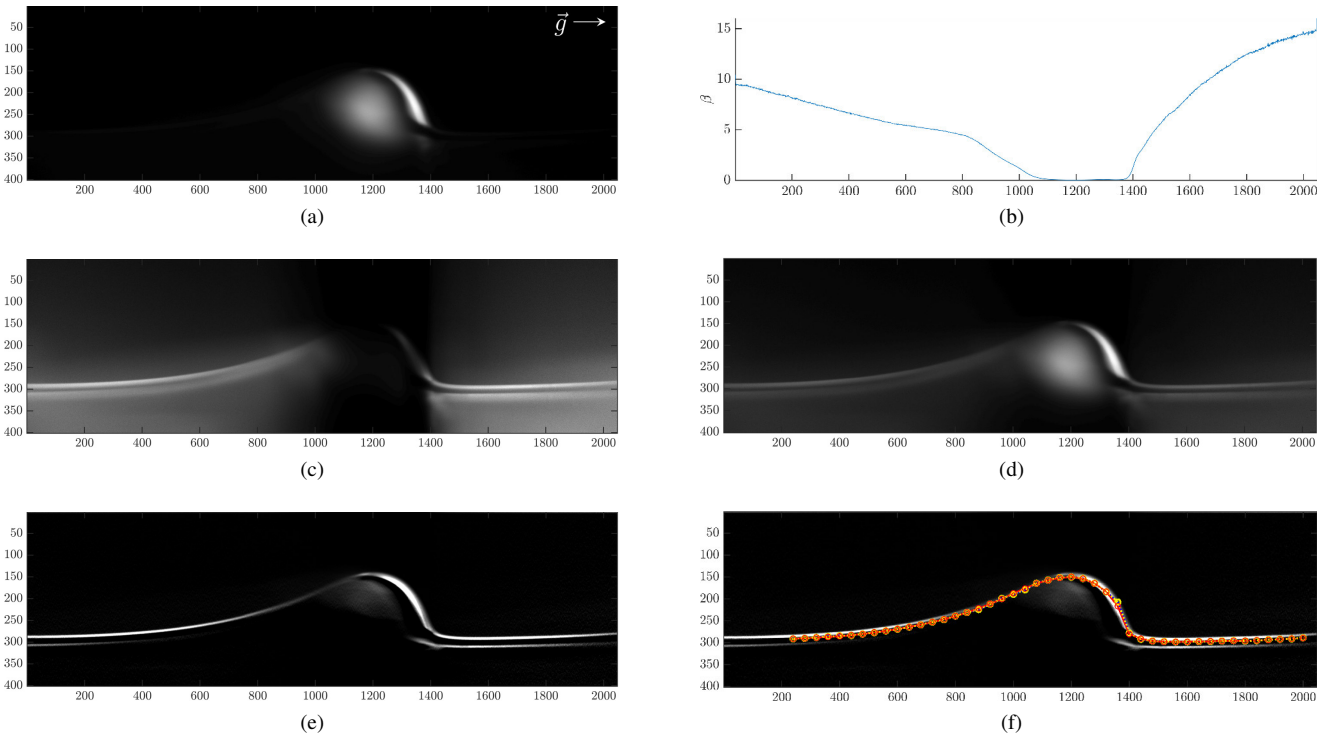

Figure 12: Image processing steps for LeDaR: From the raw image (in a), the algorithm computes the enhancement factor β (plotted in b), and use it to directionally recontrast the image. The results (in c), is added to the original image, obtaining the figure in d. Finally, a sobel-like kernel enhances the liquid interface (in e) and the column-wise peak finder method locates the interface in the image (in f).

appreciable perspective error was observed. The image processing technique proposed in this work is divided in three steps: gray scale re-contrasting, edge enhancement and edge location. The re-contrasting is used to uniform the light intensity within the liquid film, which is reduced by large waves such as in figure 12a. This step is based on a directional gray scale averaging. The idea is sketched in figure 13. Let $A(x_i, y_i) \in \mathbb{R}^2$ be the gray scale image with $x_i \in [0, n_x]$ columns and $y_i \in [0, n_y]$ rows having a mean gray scale level μ_A. Let $D = f(x_i) \in \mathbb{R}^{1\times n_p}$ be a user defined line, passing through n_p image pixels, each of which identifying an orthogonal line $P_n(x_i)$ and a gray scale profile $A(x_i, P_n(x_i))$ having average μ_n. In the directional re-contrasting step, each of the n_p gray scale profile $A(x_i, P_n(x_i))$ is multiplied by an enhancement factor of the form $\beta_n = (\mu_n/\mu_A)^k$.

In this work the stretching direction D is chosen to be horizontal, thus the gray scale profile are taken column-wise. For the image snapshot in figure 12a, the enhancing factor with $k = 2$ is plotted as a function of the image column in figure 12b. The stretching result, shown in figure 12c, improves the light uniformity in the darkest regions while causes a darkening of the brightest ones. This image is added to the original one, obtaining the image B, in figure 12d. The second step of the processing is the edge enhancement. This is done by convolving the image B with an extended Sobel-like [9x3] kernel K, which is a reduced version of the maximum forward [21x3] kernel presented in [25]:

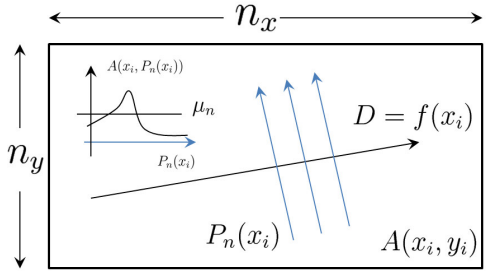

Figure 13: Working principle of the directional re-contrasting used as first step of the image processing.

$$C(x_n, y_n) = B(x_n, y_n) * \begin{pmatrix} -E \\ C \\ E \end{pmatrix} \tag{15}$$

where:

$$C = \begin{pmatrix} 0 & -1 & 0 \\ 0 & 0 & 0 \\ 0 & 1 & 0 \end{pmatrix} \quad E = \begin{pmatrix} 1 & 2 & 1 \\ 1 & 2 & 1 \\ 1 & 2 & 1 \end{pmatrix} \tag{16}$$

This operation enhances the horizontal edges of the image and results in a bright interface region with thickness varying between 4-16 pixels. The results, shown in figure 12e, is used to locate the interface position $h_p(x_i)$ in each column from the position of the peak in the profile $C(x_i, y_n)$. In particular, the peaks are detected using

standard prominence method on a smoothed version of the profiles, ensuring that the interface positioned is in the middle of the white interface band as shown in figure 12f.

4.3 LeDaR Uncertainty

The measurement uncertainty is assumed to be due to the interface location h_p in the pixel space and the scaling factor M used to convert the results in the physical units. The small and purely random uncertainty in the detection of the scaling factor M and the absence of perspective deformation during the calibration allows to neglect camera alignment uncertainties.

5 Data Scaling and Parametrization

The dynamics of a vertical falling liquid film is controlled by two dimensionless number. The natural scaling of the N-S equations leads to the Reynolds number $Re = [u][h]/\nu$ and the Weber number $We = \sigma/\rho[u]^2[h]$ were $[u]$ and $[h]$ are the reference velocity and thickness respectively. The selection of these quantities is typically based on the definition of the *Nusselt* flow, i.e. the liquid film flow obtained in steady condition assuming that the interface remains flat and constant. These two assumptions suppress the role of inertia and surface tension and the flow results from the balance of viscosity and gravity. The film thickness h_N and the corresponding mean velocity u_N are consequently linked by the liquid properties and the flow rate per unit width $q_N = h_N u_N$, thus the Reynolds number Re:

$$h_N = \left(\frac{3\nu q}{g}\right)^{1/3} = \left(\frac{3\nu^2}{g}\,Re\right)^{1/3} = l_\nu \left(3Re\right)^{1/3} \tag{17}$$

$$u_N = \frac{g h_N^2}{3\nu} = \frac{1}{3}(\nu g)^{1/3}\left(3Re\right)^{2/3} = \frac{l_\nu}{3t_\nu}\left(3Re\right)^{2/3} \tag{18}$$

where $l_\nu = (\nu^2/g)^{1/3}$ and $t_\nu = (\nu/g^2)^{1/3}$ are the viscous-gravity length and time scales. The Nusselt thickness h_N is chosen as reference length $[h] = h_N$ in the cross-stream direction whereas it is worth observing that the definition of the velocity scale $[u]$ is not unique in the literature of liquid film. In the definition of the Reynolds number it is $[u] = u_N$, whereas it is usually considered as $[u] = 3u_N$ when scaling the N-S equation (see [3] and [4]). This approach, responsible for the factor $[u]/u_N = 3$ appearing in various term of the scaled N-S, and in eq.s 17 and 18, is motivated by the willing of maintaining the standard definition of $Re = q_N/\nu$ all the while scaling the liquid film velocity with respect to the fastest waves arising from the natural interface instabilities. These are the kinematic waves arising when neglecting the non linear inertial and surface tension effects, traveling at $c_w = 3u_N$ ([2]).

Regarding the stream-wise reference length scale $[x]$, as waves in liquid films are typically long wavelength $\lambda >> h_N$, analytical models [7, 8] compress the stream-wise coordinate by a factor $k = 1/\varepsilon$, so that $\varepsilon = [h]/[x] << 1$. After Shkadov [13], this factor is typically identified by selecting the stream-wise reference length $[x]$ from the balance of capillary pressure gradient ($\approx \sigma\partial_{xxx}h$) and gravity volume force ($\rho\, g$):

$$\sigma\,\partial_{xxx}h \approx \sigma\,\frac{h_N}{[x]^3} \approx \rho\, g \rightarrow [x] = We^{1/3}h_N\,, \tag{19}$$

from which $\varepsilon = We^{-1/3}$. This reordering parameter is conveniently rewritten by replacing the Weber number We with a dimensionless number which solely depends on the liquid properties. This is the Kapitza number Ka:

$$Ka = \frac{9\,We}{(3Re)^{5/3}} = \frac{\sigma}{g^{1/3}\,\nu^{4/3}\,\rho} = \left(\frac{l_\sigma}{l_\nu}\right)^2, \tag{20}$$

being $l_\sigma = \sqrt{\sigma/(\rho g)}$ the capillary length. This number compares the importance of surface tension to viscous dispersion. Introducing eq.20 in eq.19 yields:

$$\varepsilon = \frac{(3Re)^{2/9}}{Ka^{1/3}} \tag{21}$$

For a laminar liquid film with $Re = O(10)$, the assumption of $\varepsilon \ll 1$ implies that $Ka \gg 1$. This is true for liquid such as water or alcohols ($Ka = O(10^3)$), but not for liquids such as the Dipropilene Glicole used in this work, for which $Ka = 4.61$. As result, the stream-wise length scale is $[x] \approx [h]$ and the analytical models described in [3, 4] lose their fundamental framework. The Shkadov scaling remains nevertheless the best attempt to separate the "fast" cross-stream scale from the "slow" stream-wise scale, and it is therefore used to scale the thickness measurement in this work. In particular, the flow regime is defined in terms of a *Reduced Reynolds number* δ and the *Viscous Dispersion Parameter* η:

$$\delta = 3\varepsilon Re = \frac{(3Re)^{11/9}}{Ka^{1/3}}\ ,\ \eta = \varepsilon^2 = \frac{(3Re)^{4/9}}{Ka^{2/3}}\ , \tag{22}$$

while the scaling of the film thickness variables reads:

$$\hat{h} = \frac{h}{h_N}\ \ \hat{x} = \frac{x\varepsilon}{h_N}\ \ \hat{c}_w = \frac{c}{3u_N} \tag{23}$$

6 Results

For a set of steady tests at different mean pressures, figure 14a compares the dimensionless mean film thickness measured via LAbs (red, dotted line) and LeDaR (blue, dashed line) with the theoretical Nusselt film thickness ($\hat{h} = 1$) in eq.17, where eq.5 is used to compute the Reynolds number Re from the measured mean pressure P_M. The error bars are computed as the least square of the systematic uncertainties from eq.11 and the standard deviation resulting from the spatial and temporal averaging. The amplitude of the long wavelength waves naturally developing over the mean flow remains within the systematic measurement uncertainties and do not produce increasing error bars. The good agreement between measurement and theoretical prediction validates the derivations in eq.17 and

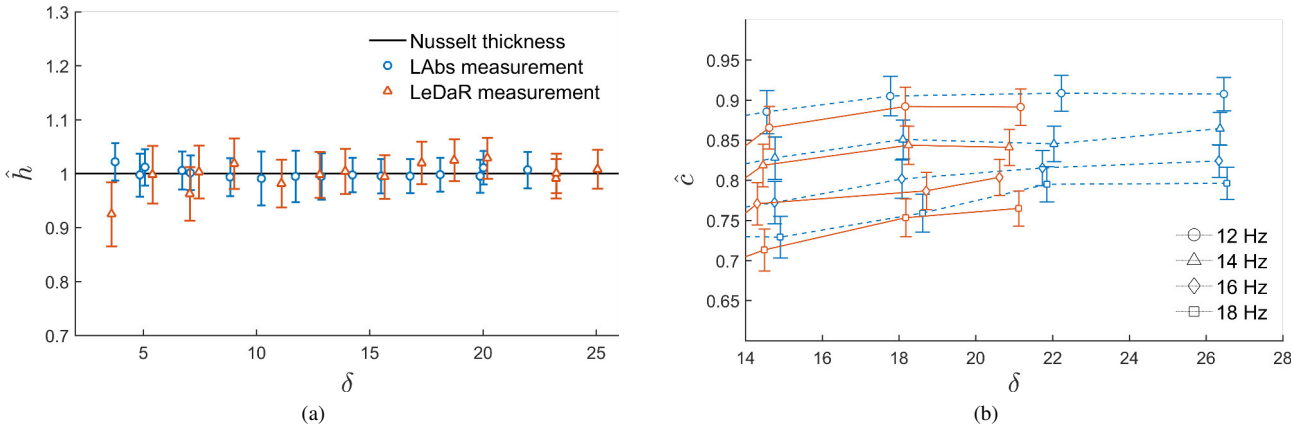

Figure 14: Deviation from Nusselt film thickness ($\hat{h} = 1$,figure 14a) as a function δ. Figure 14b: wave celerity $\hat{c}$ as a function of δ and perturbation frequencies f_p, for LeDaR (blue, dashed line) and LAbs (red, continuous line) measurements.

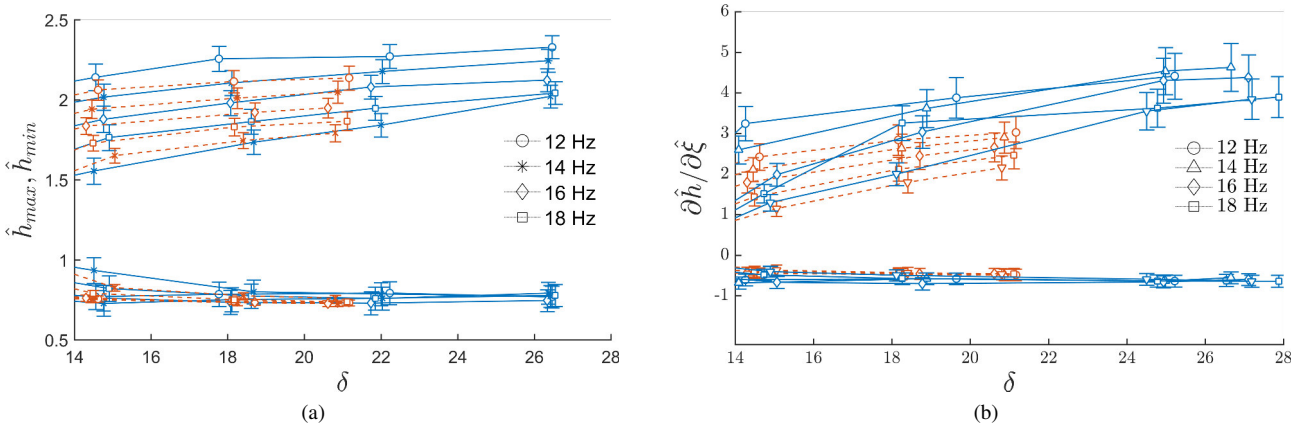

Figure 15: Minimum and maximum thickness ($\hat{h}_{min}/\hat{h}_{max}$,figure 15a) and maximum slopes ($\partial\hat{h}/\partial\hat{\xi}$, figure 15b) in the wave front and tail as a function of δ for different perturbation frequencies f_p, from LeDaR (blue, dashed line) and LAbs (red, continuous line) measurements.

eq.5, which are hereinafter used to non-dimensionalize the test cases with unsteady flow rate. The comparison between LAbs and LeDaR for the unsteady cases is carried out in the same spatial location, thus in the final portion of the LAbs measurement (see ROIs in figure 3). Figure 14b presents the wave celerity, obtained by cross-correlating the thickness profiles in two subsequence images. In the range of reduced Reynolds δ considered, both techniques show a weak dependency of the dimensionless wave celerity as a function of δ, and a more evident dependency on the perturbation frequency f_p. This is due to amplitude of the perturbation produced in the facility, as higher frequency, thus high $\mathcal{W}$, leads to stronger inertial damping, thus smaller perturbation strength $\zeta = Re_A/Re_M$, as shown in figure 5. Figure 15a shows the evolution of wave maxima and minima as function of δ for several perturbation frequencies f_p. While the wave peaks grow monotonically, the wave minima exhibit an asymptotic behavior towards $\hat{h}_{min} \approx 0.75$, regardless of perturbation amplitude and frequency. A fair agreement in both techniques is observed.

Figure 15b shows the evolution of the maximum thickness slope $\partial_{\hat{\xi}}\hat{h}$ in the front and in the tail of the waves. These gradients are computed from the wave profiles extracted in the moving reference frame ($\hat{\xi} = \hat{x} - \hat{c}\hat{t}$), shifted to have the wave peak at $\hat{\xi} = 0$. For plotting purposes, we assign a positive sign to the tail's slope, a positive sign to the front's slope. In the latter, a systematic discrepancy between the two techniques is evident, with the LeDaR detecting higher values than the LAbs. This discrepancy is due to a different prediction of the wave profile in the wave front. Figure 16 and figure17 show several dimensionless profiles for LAbs and LeDaR, at $12Hz$ and $18Hz$ respectively, for different mean Reynolds number. Besides the difference in the peaks, due to the slight difference in the mean Reynolds, the profiles detected in the LeDaR have a curvature in the front which is not observed in those detected in the LAbs. Such difference increases with the wave peak, thus the interface curvature, and it is due to light refraction in the wave front, which biases the LeDaR measurements. Finally, it is worth noticing, in the profiles obtained with both techniques, the absence of capillary ripples in the front wave. These ripples, typical of high Ka liquids, are damped in low Ka liquids by the high

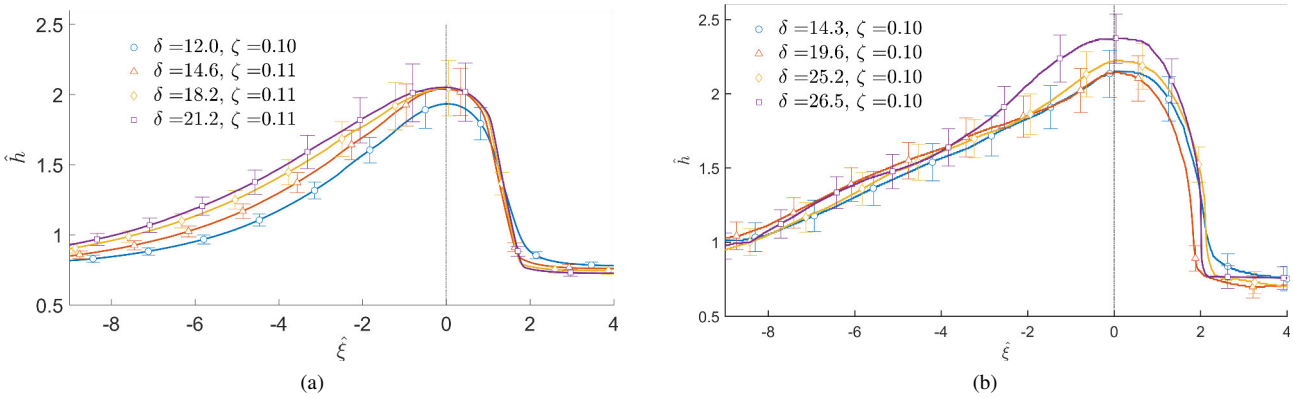

(a) (b)

Figure 16: Wave profiles obtained via LAbs (figure 17a) and LeDaR (figure 17b) at different Reynolds number δ and perturbation strength ζ, for a perturbation frequency $f_p = 12Hz$.

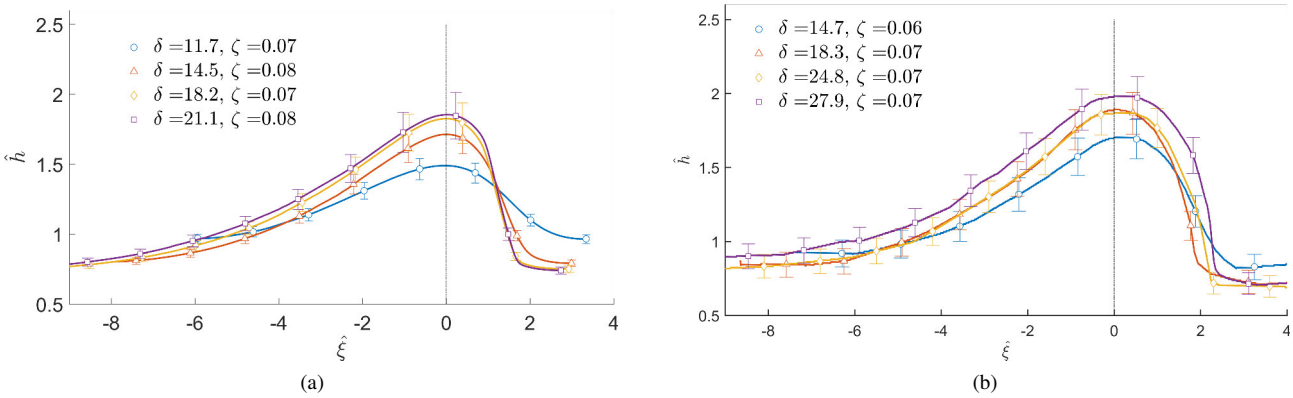

(a) (b)

Figure 17: Wave profiles obtained via LAbs (figure17a) and LeDaR (figure 17b) at different Reynolds number δ and perturbation strength ζ, for a perturbation frequency $f_p = 18Hz$.

viscous dispersion, which is of the same order of magnitude of surface tension ($\varepsilon \approx \eta \approx 1$).

7 Conclusions

This paper has presented film thickness measurements, using Light Absorption and Laser Tomography, on a vertical falling liquid film with low Kapitza number. Unperturbed (steady) and perturbed (pulsing) flow rates have been considered. For both techniques, calibration, uncertainty, and processing aspects have been discussed in detail. In the steady tests, the results show excellent agreements between the techniques in terms of mean film thickness, recovering the Nusselt film theory. In the unsteady tests, the techniques agrees in the measurement of wave celerity and thickness maxima and minima, with a slight discrepancy in the wave profiles, particularly in wave front.

Acknowledgments

M. A. Mendez is supported by an F.R.S.-FNRS FRIA grant and the research program is funded by Arcelor-Mittal. The authors gratefully acknowledge the contributions of Dr. Flora Tomasoni in the design and the preparation of the experiments and the fruitful discussions with Prof. B. Scheid, from ULB University, concerning the modeling and the scaling of liquid film flows.

Nomenclature

Notation

$[x]$	Characteristic scale for x
$\hat{x}$	Nondimensionalized x -
x_A	Oscillating amplitude of x
x_M	Mean component of x
$\mathcal{U}_x$	Uncertainty of x

Dimensionless Quantitites

Re	Reynolds number
Ka	Kapitza number
$\mathcal{W}$	Womersley number
$\mathcal{T}$	modulation factor
ζ	perturbation strength
δ	reduced Reynolds number
ϵ	ordering parameter
η	viscous dispersion parameter

Dimensional Quantities

A	Absorbance coefficient	-
b	channel half opening	m
β_n	contrast enhancing factor	-
c	colourant concentration	mg/kg
c_w	wave celerity	m/s
f_p	perturbation frequency	Hz
f_s	sampling frequency	Hz
γ_g	global absorption coefficient	$1/mm$
H	hydrostatic head	m
h	film thickness	m
I_0	reference image	$graycounts$
I	transmittance image	$graycounts$
L	channel length	m
l_σ	capillary length scale	s
l_v	viscous length scale	s
M	image scaling factor	$pixel/mm$
μ	dynamic viscosity	$Pa\ s$
μ_m	gray scale average along P	$Pa\ s$
M	image scaling factor	$pixel/mm$
n_t	number of images	
$n_{x/y}$	image size	$pixels$
ν	kinematic viscosity	m^2/s
ω	angular frequency	rad/s
P	total pressure	Pa
p	gauge pressure	Pa
P_n	image profile direction	$pixel$
ρ	density	kg/m^3
q	flow rate per unit width	m^2/s
σ	surface tension	mN/m
t_v	viscous time scale	s
u	stream-wise velocity component	m/s
ξ	traveling reference frame	m

References

[1] Kapitza, P.L., Kapitza, S.P, Collected Papers of P.L. Kapitza, **II**, (1938-1964), Pergamon Press, pp. 662–709.

[2] Alekseenko, S.V., Nakoryakov, V.E., Pokusaev, B.G., *Wave Flow of Liquid Films* (Begell House,1994).

[3] S. Kalliadasis, S., Ruyer-Quil, C., Scheid, B., Velarde, M.G., *Falling Liquid Films*, Vol. 176 (Springer, 2012).

[4] Ruyer-Quil, C., Kofman, N., Chasseur, D., Mergui,S., Eur. Phys. J. E **37** (30), (2014).

[5] Alekseenko, S.V., Nakorykov, V.E., Pokusaev, B.G., Int.J.Multiphase Flow, **11** (5), (1985) pp. 607-627.

[6] Chang, H.-C., Annu. Rev. Fluid Mech. **26**, (1994) pp. 103-136.

[7] Scheid, B., Ruyer-Quil,C., Manneville, P. , J. Fluid. Mech **531**, (2005) pp. 181-190.

[8] Scheid, B., Ruyer-Quil,C., Manneville, P. , J. Fluid. Mech **562**, (2006) pp. 183-222.

[9] W.B. Krantz, S.L. Goren, Ind. Eng. Chem. Fundam. **10**(91) (1971).

[10] Moran, K., Inumaru, J., Kawaji, M., Int. J. Multiphase Flow **28**(5) (2002).

[11] L. T. Nguyen, V. Balakotaiah, Phys.Fluids, **12**(2236) (2000)

[12] Charogiannis, A., An, J.S., Markides, C.N., Exp. Therm. Fluid Sci., 68, (2015).

[13] Shkadov, V. Y., Izv. Akad. Nauk SSSR, Mekh. Zhidk Gaza **1**(63), (1977) pp. 29-34.

[14] Lilleleht, L.U., Hanratty T.J., J. Fluid Mech **11**, (1961), pp. 65-81.

[15] Stainthorp,F.P., Allen,J.M. Trans.Inst.Chem.Engrs **43**(3), (1965), pp. 85-91.

[16] Portalski,S., Chem.Eng.Sci. **18**, (1963), pp. 787-804.

[17] Özgen, S., Carbonaro, M., Sarma, G.S.R, Phys. Fluids **14**, (2002), pp. 3391-3420.

[18] Gosset, A., in *Thermohydraulic Instabilities*, VKI Lecture Series 2006-07, pp 1 - 25.

[19] Njifenju, A.K., Bico, J., Andrés,E., Jenffer,P., Fermigier, M. Exp. Fluids **54** (1506), (2013), pp. 3391-3420.

[20] Driscolli,D.I., Schmitt,R.M., Stevenson, W.H. J.Fluids Eng. **114**, (1992), pp. 107-112.

[21] Liu,J., Schneider J.B., Gollub J.P., Phys.Fluids **7**(1), (1994), pp. 55-67.

[22] Liu,J., Gollub J.P., Phys.Fluids **6**(5), (1994), pp. 1702-1712.

[23] D. Bouchez, D., Zimmer, L., Reithmuller, M.L. Proceedings of the 9th Symp. of Flow Visualization, (2000), Edinburgh, SCT.

[24] Planquart, Ph., Proceedings of the 4th European continuous casting conference, (2002), Birmingham, UK.

[25] Toth, B., Anthoine, J., Reithmuller, M.L. Congres Francophone de Techniques Laser, (2006), Touluse, FR.

[26] Toth, B., Ph. D. thesis, Free University of Bruxelles, Brussels, Belgium, (2008).

[27] Hewitt, G.F., Jayanti, S., Hope, C.B., Gingell, D., Int. J. of Multiphase Flow **16**(6), (1990), pp. 951-957.

[28] Ursenbacher, T., Wojtan, L., and Thome., J. R., Int. J. of Multiphase Flow **30**(2), (2004), pp. 107-124.

[29] Wojtan, L., Ursenbacher, T., and Thome., J. R., Int. J. of Multiphase Flow **30**(2), (2004)(2), pp. 125-137.

[30] Rodriguez, D. J., Shedd, T.A., ASME Heat Transfer/Fluids Eng. Summer Conference, (2006) Charlotte, NC, USA.

[31] Farias, P.S.C., Martins, F.J.W.A., Sampaio, L.E.B., Serfaty, R., Azevedo, L.F.A., 15th Int. Symp. on Applications of Laser Techniques to FLuid Mechanics, (2010) Lisbon, PT

[32] Womersley, J.R., J. Physiol., 127 (1955).

[33] Rohlf, K., Tent, G., Journal of biomechanics, 34(1) (2000)

[34] Loudon, C., Tordesillas, A., J. Theor. Biol., 191(1) (1998)

[35] Karagoz, I., Uludag Universitesi MMFD, 7 (2002)

[36] Mendez, M.A., von Karman Institute, TN 215 (2015).

[37] Garcia, D., Comput. Stat. Data Anal. 54 (2010).